Electronic Properties of Functionalized Diamanes for Field Emission Displays

Christian Tantardini[1,2], Alexander G. Kvashnin[3], Maryam Azizi[4], Xavier Gonze[,4], Carlo Gatti[5], Tariq Altalhi[6], Boris I. Yakobson*[2,6]*

[1]*Hylleraas Center, Department of Chemistry, UiT The Arctic University of Norway, P.O. Box 6050 Langnes, N-9037 Troms., Norway*

[2]*Department of Chemistry, Rice University, Houston, Texas 77005, United States of America.*

[3]*Skolkovo Institute of Science and Technology, 121205, Bolshoi Blv. 30, Building 1, Moscow, Russian Federation.*

[4]*Université catholique de Louvain, Place de l'Université 1, 1348, Ottignies-Louvain-la-Neuve, Belgium.*

[5]*CNR - Consiglio Nazionale delle Ricerche, SCITEC - Istituto di Scienze e Tecnologie Chimiche "Giulio Natta", sezione di via Golgi, 19, 20133 Milan, Italy.*

[6]*Chemistry Department, Taif University, Al Hawiyah, Taif 26571, Saudi Arabia.*

ABSTRACT. Ultrathin diamond films, or diamanes, are promising quasi-2D materials which are characterized by high stiffness, extreme wear resistance, high thermal conductivity, and chemical stability. Surface functionalization of multilayer graphene with different stacking of layers could be an interesting opportunity to induce the proper electronic properties into diamanes. Combination of these electronic properties together with extraordinary mechanical ones will lead to their applications as field-emission displays substituting original devices with light-emitting diodes (LEDs) or organic light-emitting diodes (OLEDs). In the present study, we focus on the electronic properties of fluorinated and hydrogenated diamanes with (111), (110), (0001), $(10\bar{1}0)$, and $(\bar{2}110)$ crystallographic orientations of surfaces of various thickness by using first-principles calculations and Bader analysis of electron density. We see that fluorine induces occupied surface electronic state, while hydrogen modifies occupied bulk state, and induces also unoccupied surface states. Furthermore, a lower number of layers is necessary for hydrogenated diamanes to achieve the convergence of the work function in comparison with fluorinated with exception of fluorinated (110) and $(\bar{2}110)$ that achieve rapidly the convergence and have the same behavior than other hydrogenated surfaces. This induces a modification of the work function with increase of number of layers that makes hydrogenated $(\bar{2}110)$ diamane the most suitable surface for field emission displays, better than the fluorinated counterparts. In addition, a quasi-quantitative descriptor of surface dipole moment based on Tantardini-Oganov electronegativity scale is introduced as the average of bond dipole moments between the surface atoms. This new fundamental descriptor is capable to predict a priori the bond dipole moment and may be considered as a new useful feature for crystal structure prediction based on artificial intelligence.

KEYWORDS: Diamanes, 2D structures, TB09, Abinit, meta-GGA, GW approximation, Bader theory, Tantardini-Oganov electronegativity, field-emission displays.

Introduction

Nowadays, the possibilities of applications of two-dimensional materials for electronic devices are scrutinized by numerous research groups worldwide. The search for new materials for application in field emission displays (FEDs) represents a very hot topic due to the necessity to produce flatter panels (i.e., approximately 2 mm) with the characteristics to be self-emissive distortion-free images and wide view angle (i.e, about 170 degrees). Furthermore, field-emission displays are characterized by quick response, in the order of microseconds, tolerance to environments as high as that of receiving tubes, and free from terrestrial and applied magnetic effects [1–6]. These characteristics make FEDs more appreciated than corresponding light-emitting diodes (LEDs), organic light-emitting diodes (OLEDs), and surface-conduction electron-emitter displays (SED) [1–6]. The search for new materials employed as FEDs benefits enormously from a deep study of the electronic structure at the surface, that in most cases is peculiar and differs from the bulk, due to significantly changed chemistry caused by the surface modified bonding pattern.

Considering carbon materials one notes that diamond and lonsdaleite are both sp^3-hybridized insulating allotropes, while their 2D counterpart – graphene [7,8] is a semimetal with sp^2-hybridized carbon atoms. Indeed, the hybridization plays an important role not only in the chemistry, but also in the electronic properties of carbon materials. In particular, the surface functionalization of multilayer graphene with different stacking of layers by different atoms enables chemically induced phase transition converting multilayer graphene into diamond-type structure with sp^3-hybridized carbon atoms in all layers leading to semiconducting properties [9–17]. These functionalized multilayers are different from graphene, that present sp^2 hybridization of carbons and electronic properties of a semi-metal. The sp^3-hybridized multilayers are quasi-2D compounds called diamanes, various structures of which are caused by AA-, AA′ or AB-stackings of graphene layers [9,11–17]. More exotic structures can be formed by fabrication of Moiré patterns from bilayer graphene functionalized by hydrogen or fluorine [16,18–22], and even quasicrystals can be formed [23].

Indeed, the formation of diamanes from multilayer graphene via the application of low temperature and pressure (~50 Torr) was observed experimentally in Refs. [24,25]. Authors applied the hot-filament process for the efficient hydrogenation and dehydrogenation of few-layered graphene and the subsequent formation of crystalline and ultrathin sp^3-carbon sheets.

Diamanes exhibit a unique combination of physical properties such as high thermal conductivity [26–31], which is compatible with small-polaron charge carrier, and optical characteristics [32–34] making them suitable for potential applications in electro-mechanical devices [30]. In addition, diamanes with different functionalization of surfaces could be good

candidates for FEDs. Indeed, 2D materials are also remarkable due to the possibility to dope their surface in a reversible way by functionalization/defunctionalization. Hence the switching of electronic properties from metal to semiconductor and vice versa occurs due to the chemical or photo-chemical reactions. A sort of reversible photo-doping was recently discovered by Gierster et al. [35] at the $(10\bar{1}0)$ surface of ZnO, where phase transition is caused by photoinduced downward surface band bending due to photodepletion of donor-type deep surface defects.

Hydrogenated diamanes is a case of reversible chemical doping[24,36–39]. Furthermore, reversible fluorination of few-layer graphene was also experimentally achieved in Refs. [40–43]. Actually, for both hydrogenated and fluorinated diamanes the energy barrier of hydrogenation or fluorination decreases with the number of layers and the monolayer[13,14,44].

Thus, to understand the possibility of using diamanes in FEDs, a state-of-the-art fundamental study of their electronic properties with first-principles calculations is much needed, which is the goal of the present work. Indeed, Kohn-Sham (KS) electronic band structure together with *GW* approximation gap values [45] allow us to understand the dependence of the work function on the functionalization type and thickness of diamanes. A subsequent study of electron population at the valence band maxima (VBM) within the framework of Bader theory [46,47] applied for 2D materials [48,49] enables us to understand the atomic contribution responsible for the conductivity making clear the electronic transport behavior at the atomistic level in view of the future development of 2D opto-electronic devices based on diamanes.

Results and discussion

Five types of diamanes are considered, having (111), (110), (0001), $(10\bar{1}0)$, and $(\bar{2}110)$ crystallographic orientations of surfaces, with thickness from 1 to 6 layers, and hydrogen- or fluorine-functionalization, so altogether 60 structures. Hydrogen and fluorine atoms are bonded with the surface carbon atoms through a covalent bond. Thus, all carbon atoms in the considered diamanes are sp^3-hybridized. Atomic structures of these five types of diamanes are shown in Figure 1. Diamanes with (111) and (110) surfaces belong to a group of films with cubic diamond structure type, while other films have lonsdaleite (hexagonal diamond) structure type. Yellow atoms in Figure 1 represent non-carbon atoms (hydrogen or fluorine, which are presented here). Films with (0001) and $(\bar{2}110)$ surfaces can be formed by passivation of graphene multilayers with AA stacking, while AA' stacking leads to formation of $(10\bar{1}0)$ films[12].

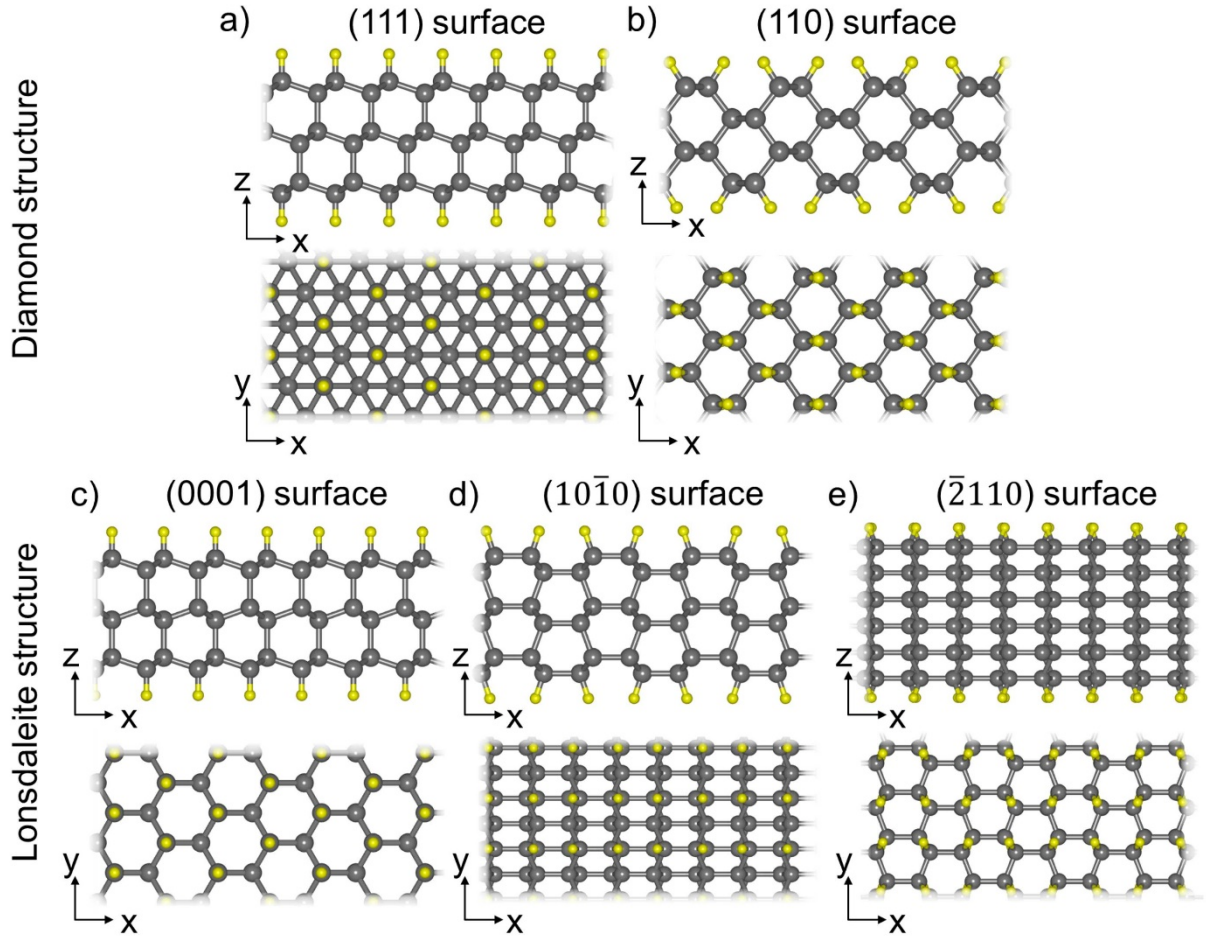

Figure 1. Top and side views of atomic structures of the considered diamanes with diamond and lonsdaleite structures having a) (111), b) (110), c) (0001), d) $(10\bar{1}0)$, and e) $(\bar{2}110)$ surfaces respectively. Grey balls represent carbon atoms; yellow balls are non-carbon atoms (H or F).

For each considered diamane, the Kohn-Sham (KS) electronic band structure is calculated by using the TB09 (aka modified Becke-Johnson, a meta-GGA functional) DFT exchange-correlation functional[50], on top of an GGA-PBE optimized structure, as shown in Figure S1-S10 in the Supporting Information. The TB09 functional is quite efficient in calculating the accurate band gap of various bulk materials, with respect to LDA and GGA-PBE, and is in a reasonable agreement with the *GW* approximation or experimental data for bulk solids [50–52]. This makes it a priori an excellent starting point to achieve useful information about electronic band structure and band gap for 3D structures [53] and we will test it here on 2D structures.

All hydrogenated (111), (110), (0001), $(10\bar{1}0)$, and $(\bar{2}110)$ diamanes possess direct TB09 KS band gap (Figure S1-S10 in Supporting Information). Few-layer fluorinated (111), (110), (0001), $(10\bar{1}0)$ diamanes are characterized by direct band gap, while increase in thickness leads to appearance of an indirect band gap, with exception of $(\bar{2}110)$, which is a direct gap semiconductor

for all considered thicknesses (Figure S1-S10 in Supporting Information). As we know the band gap analysis gives a crucial information about the system. However, the accuracy of KS electronic band structure is affected by the DFT problem that underestimate the band gap, and overestimates the electronic repulsion with the Hartree term, that is not always properly balanced with the exchange-correlation functional.

To evaluate the quantitative prediction of band gaps in 2D solids obtained with TB09 we have subsequently performed G_0W_0 calculations on top of the TB09 DFT functional (from now on, referred to as *GW*@TB09). Furthermore, we have compared fundamental and direct gaps obtained with *GW*@TB09 as a function of the inverse squared number of layers (see Figure 2 and Figure S11 in Supporting Information). This was done according to the fact that in quantum mechanics the energy level spacing of a particle in a square box (like a confined electron) is a function of the inverse squared box size. Theoretically, an increase in the number of layers (L) of diamanes should lead to a decrease in the band gap until converging to the value for bulk lonsdaleite or diamond in the limit of $L\rightarrow\infty$. In reality, such behaviour is preserved for bulk states, but modifications do not follow the same law for surface state(s).

Moreover, comparing the *GW*@TB09 (see Figure 2) with TB09 (see Figure S11 in Supporting Information) band gap dependencies we observe two totally different behaviours. Both fundamental and direct band gaps of all hydrogenated diamanes calculated by TB09 decrease with increase of the number of layers and starting from 3 layers band gaps start to increase, Figure S11a,b. Fluorinated films demonstrate non-monotonic behaviour of band gaps with thickness (Figure S11c,d). Interestingly that band gap behaviour of $(\bar{2}110)$ diamanes is counterintuitive, namely there is no tendency to the band gaps of bulk lonsdaleite with $L\rightarrow\infty$. More accurate *GW*@TB09 corrects this situation, Figure 2. In order to double-check our *GW*@TB09 predictions, we examined whether there might be a reordering of electronic bands calculated by TB09 and G_0W_0 that might change the electronic states in hydrogenated (111), (110), (0001), $(10\bar{1}0)$, and $(\bar{2}110)$ diamanes at the band gap extrema. We have monitored the energy difference between the bands at valence band maxima with respect to the closest highest bands, confirming that no reordering occurs. Thus, while TB09 is considered as one of the best choice for KS band structure for 3D materials [53], for 2D systems its predictive capability seems degraded.

From our *GW*@TB09 results (see Figure 2) the increase of number of layers in hydrogenated diamanes always induces a decrease of band gap from its initial value (monolayer, graphene). At variance, in the fluorinated diamanes, the band gap is seen to initially increase with the number of layers from the monolayer and subsequently decrease after three layers, to converge, in the larger

thickness, to the corresponding band gap of bulk counterpart. Furthermore, only hydrogenated ($\bar{2}110$) has clearly a band gap behaviour that does not converge to the band gap of lonsdaleite with the increase of the number of layers (blue curves in Figure 2).

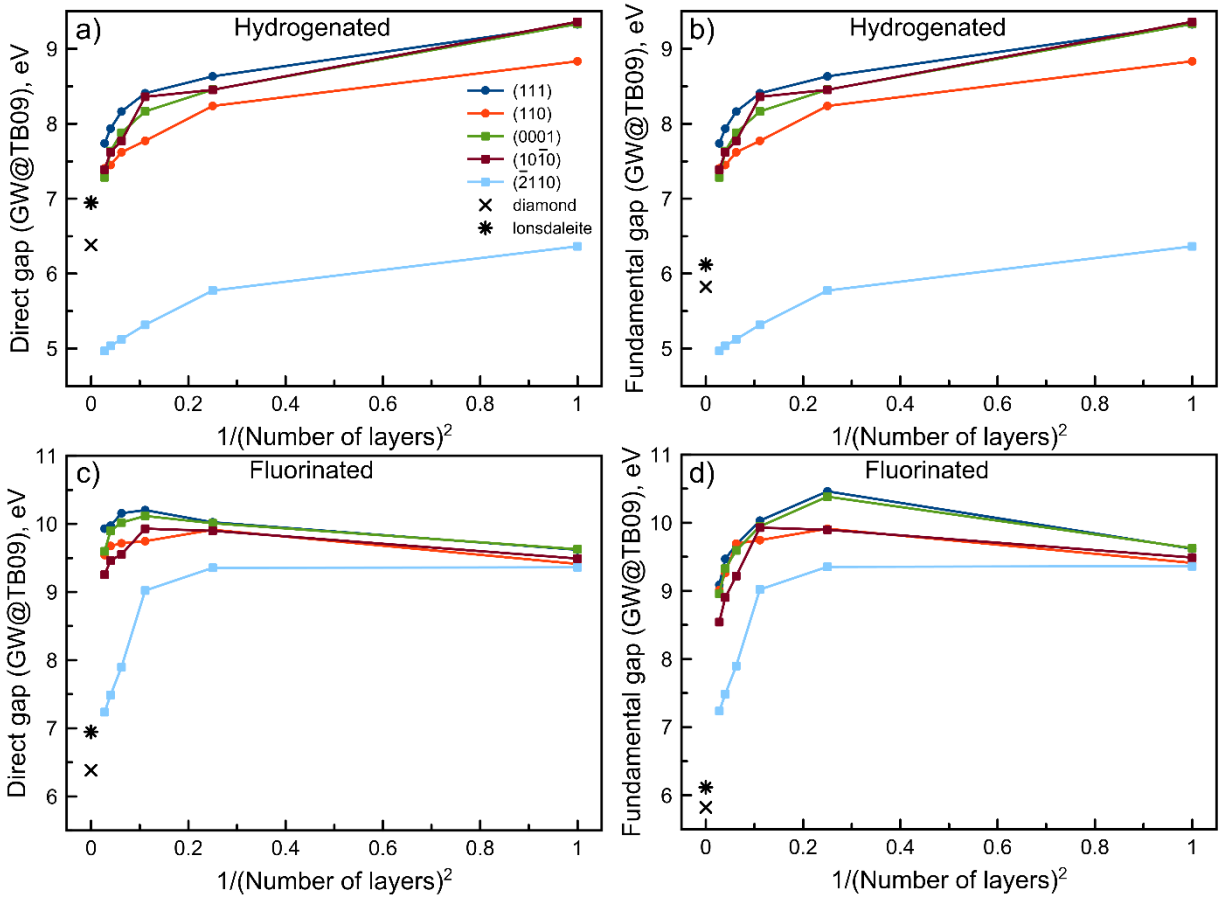

Figure 2. Dependency on the squared inverse number of layers (thickness) of the direct - a), c) - and fundamental - b), d) - band gap for hydrogenated - a), b) - and fluorinated - c), d) - diamanes, calculated by the *GW*@TB09 approach.

The band gap behaviour is affected by different functionalization of the surfaces, which are correlated with the electronic state. This can be understood by looking at the KS electronic band structures (Figure S1-S10 in Supporting Information) that is not affected by reordering, as was checked previously with *GW* calculations. KS TB09 electronic band structures (see in Supporting Information Figure S1-S10) are intricate and benefit from further investigation using Bader Theory.

Bulk electronic states in such multilayers are characterized by Bloch character of the wavefunction in the inner layers, while decaying exponentially into the vacuum. Instead, surface electronic states are characterized by exponential decay both in the vacuum and in the inner layers and thus

represents states localized at the crystal surface.

These two types of states, from the occupied bulk valence states and from the occupied surface states, contribute to the charge density of the bulk and surface with different atomic characteristics.

Actually, in presence of few layers it is difficult to speak about localized surface electronic states, because the whole few-layer structure is made of the surface. Thus, the localization can come only in presence of thicker multilayers. Thus, we can suppose that the different band gap behaviour for fluorinated and hydrogenated diamanes with the increase of layers is due to the formation of surface electronic states in one case and due to bulk electronic states in the other.

Two different electronic states can be recognised by different electronic atomic contribution to the VBM: an electronic atomic contribution coming from all bulk atom is responsible for a bulk state; an electronic contribution coming for specific localized atoms is responsible for a surface electronic state. This can be quantified through a Bader analysis.

In the case of surface electronic states, the charge density at the VBM might come from surface adatoms, as well as from the carbon atoms adjacent to these. The latter is responsible for the variation of electronic distribution within multilayer with a conductivity that does not depend on the excitation of electrons from the surface adatoms.

Hence, Bader theory [46] provides a detailed characterization of the surface and bulk electronic states in diamanes with different functionalization, and provide a partition of the charge in different atomic contributions. In such theory (also called QTAIM, *i.e.* quantum theory of atoms in molecules)[46], the atoms are not considered as spherical units intrinsically defined and independent by the context, but their shape and volume is strongly influenced by the surrounding atoms. Atoms in molecules are defined as atomic basins delimited by the so-called zero flux surface. Such surface is made by the infinity of points $\mathbf{r}$, for which the dot product of the gradient of electron density, $\nabla\rho$, and the normal vector to the surface, $\hat{\mathbf{n}}$, is zero (zero-flux boundary condition, $\nabla\rho(\mathbf{r}) \cdot \hat{\mathbf{n}}(\mathbf{r}) = 0$). We have calculated the charge density at the VBM and integrated such density within Bader atomic basins bounded by zero-flux surfaces calculated with the full electron density.[46] This was done for the six-layer diamanes. It is seen that hydrogenated diamanes states, close to the top of valence band, are predominantly bulk electronic states, while fluorinated diamanes possess important localized surface electronic states, see Figure 3, Figure S12, and Table S15 in Supporting Information.

198 Let us have now a look in detail at the diamane with $(\bar{2}110)$ surface (Figure 3) which is the
199 characteristic multilayer showing two different band gap behaviours as a function of the
200 functionalization type (fluorine or hydrogen). As can be seen by the KS band structures in Figure
201 3a,b, where the electronic band structures calculated by TB09 are shown: bulk and surface
202 electronic states are observed for hydrogenated and fluorinated diamanes respectively.

203 Now we explain in detail the fluorinated (Figure 3a) and hydrogenated diamanes with $(\bar{2}110)$
204 surfaces (Figure 3b) to rationalize the correlation between the KS electronic band structure and the
205 band population from the VBM to the inner bands.

206 The KS electronic band structure of fluorinated diamanes (Figure S2, S4, S6, S8, S10 in Supporting
207 Information) shows surface electronic states that are supported by population of VBM and first-
208 inner bands is characterized by surface fluorine atoms and their bonded carbon atoms (Figure 3a).
209 As we look in deeper bands the contribution of carbon atoms to the electronic population becomes
210 predominant (Figure 3a). The same kind of band population is shown by the Bader analysis for the
211 other structures (Figure 3c).

212 The KS electronic band structure of hydrogenated diamanes (Figure S1, S3, S5, S7, S9 in
213 Supporting Information) shows bulk electronic states that are supported by spreading of hydrogen
214 atomic charge density into the inner bands with a charge density at the VBM dominated by the
215 atomic charge density of carbon atoms as showed (Figure 3b, d).

216 The $(\bar{2}110)$ hydrogenated diamane shows a pronounced difference between conduction band
217 minima (CBM) and the first closest higher conduction band. This is responsible for such different
218 band gap behaviour seen in Figure 2 with respect to the hydrogenated diamanes with other surfaces
219 showing similar energy difference between CBM and the higher conduction bands.

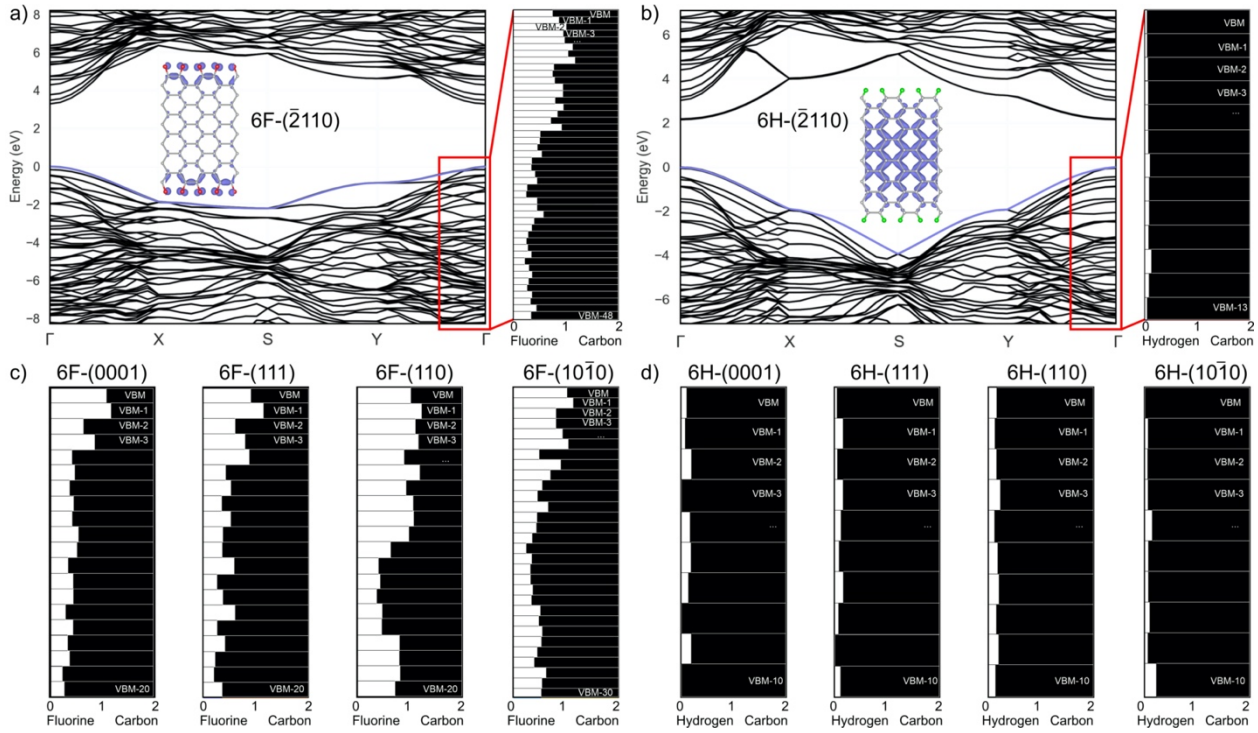

Figure 3. Electronic band structures of six-layer $(\bar{2}110)$ diamanes functionalized by a) fluorine and b) hydrogen, calculated with TB09. The insets show the charge density isosurface of electrons localized at the VBM. The isosurface value for fluorinated diamane is 0.0068 e/Å^3; for hydrogenated diamane the isosurface value is 0.0045 e/Å^3. Electronic band coloured in blue corresponds to the VBM for which the charge density is plotted for both fluorinated and hydrogenated diamanes. The right panels show the ratio of atomic population of fluorine/hydrogen and carbon atoms from the VBM to lower bands. Similar plots are shown for the atomic population for the other crystallographic orientations (111), (110), (0001), $(10\bar{1}0)$ of c) fluorinated and d) hydrogenated diamanes from the VBM to the lower bands.

As the difference between surface and bulk states at band edges affects the properties at the surface in different ways, we have calculated the work function from PBE (see Supporting Information Figure S13 and Table S13) and *GW*@PBE (see **Error! Not a valid bookmark self-reference.** and Supporting Information Table S13), depending on the number of layers, to understand how many layers are necessary to obtain a promising FED.

Indeed, we have observed a different work function behaviour after *GW* correction that significantly shift the VBM respect to PBE results as expected for the band gap results obtained with *GW* correction on top of TB09.

The work function values of fluorinated diamanes are larger than that of hydrogenated ones and linearly decreases except for (111) and (0001) surfaces where the work function displays behaviour similar to the band gap dependence, namely the work function increases from monolayer to three-layers and then decreases. This is coherent with the formation of local surface states in the case of

multilayers, that for such structure also affect the work function behaviour. Furthermore, the F-($\bar{2}$110) diamane has the same behaviour than H-(111), H-(110), H-(0001), and H-(10$\bar{1}$0) films, although having higher work function than hydrogenated ones for thin films, see Figure 4. It monotonically decreases with the increase of number of layers, reaching ~ 6 eV at 6 layers.

The *GW* correction singles out the hydrogenated ($\bar{2}$110) surface, that has the lowest work function values, starting from ~6.5eV for the monolayer, decreasing with the number of layers, and achieving ~3.5 eV for 6 layers.

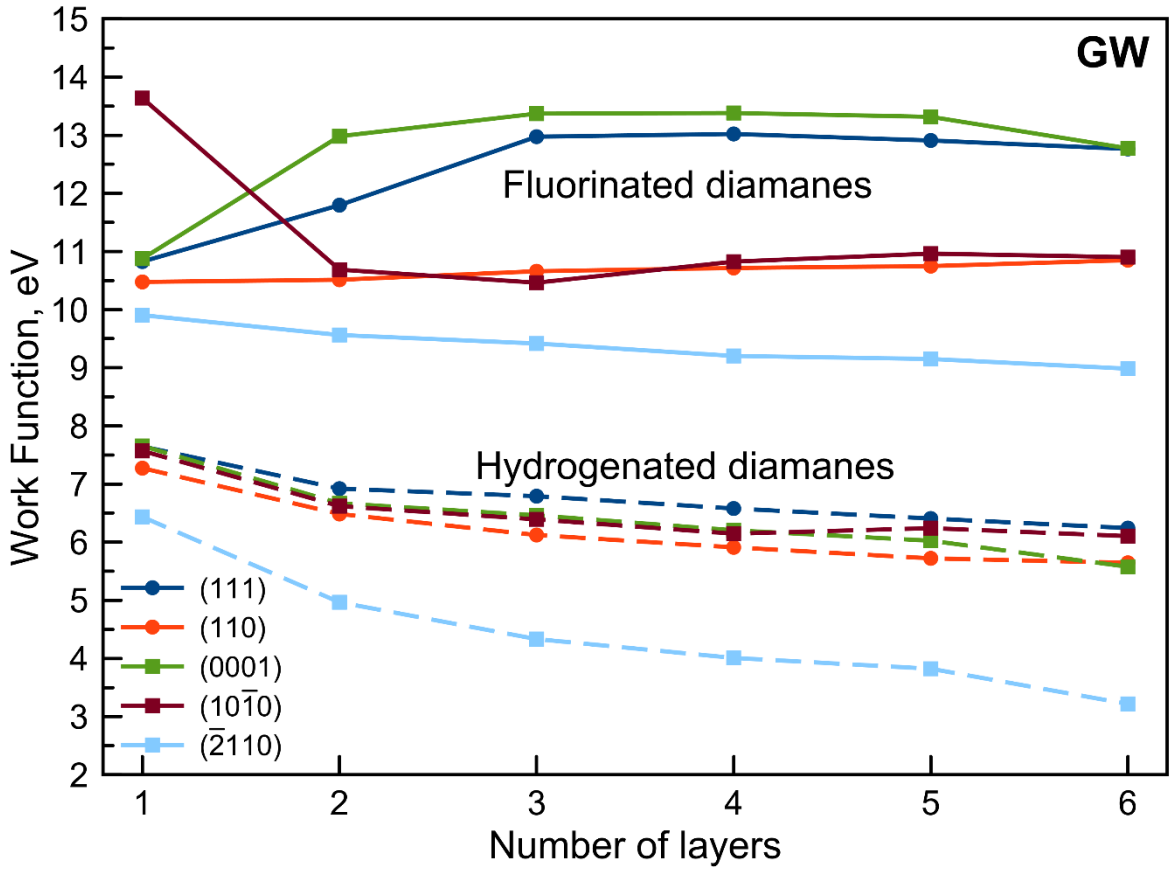

Figure 4. Work function depending on the number of layers for considered fluorinated and hydrogenated diamanes with different orientation of surfaces obtained by *GW*@PBE.

An additional concept that we analysed in our work is the dipole moment in 2D materials to understand the intrinsic electronic properties of diamanes. Usually, in 2D materials one evaluates the surface dipole moment, which describes the transfer of charge that happens at the interface between the edge of material and the vacuum when a fictitious potential is applied. To describe the charge distribution at the surface different models were previously developed: the Helmholtz model, where an electric double layer consisting of two oppositely charged layers is assumed, and where the charges on the surface of material form a pearl necklace (i.e., uniform distribution)

where charges are free to move[54]; the Gouy-Chapman model, where the interfacial potential is created, like in the Helmholtz model, with the difference that the charges in the vacuum are not free to move and are in the same number and opposite in sign to those of the surface of material[55,56]; the Stern model, which suggests a hybrid model between two previously described, with ions that have finite size, so they cannot approach the surface closer than a few nanometers[57].

Unfortunately, these classical models fail to describe the experimental data and cannot describe the formation of dipole moments at the interface. Furthermore, these kinds of models do not deliver any intrinsic information about the electronic properties of materials.

Now, if we focus on the effects on the electronic properties simply due to the functionalization of the surfaces of diamane, then the chemical bonding between carbon and surface adatoms will be characterized by the formation of a bond dipole moment, whose intensity depends on the different electronegativities of elements. These bond dipole moments appearing between carbon and surface adatoms will be responsible for the charge separation at the surface of the film determining the intrinsic electronic properties of that functionalized material. Thus, the direction of each bond dipole moment at the surface will characterize the chemical properties of material at the atomistic level. If a bond dipole moment between carbon and surface adatoms is directed towards the deep layers or out from the material, then the electron affinity of the surface will change together with the chemical reactivity.

Hence, as we know, the bond dipole moment is defined as[58]

$$\mu_D = \delta d$$

where δ is the difference between the partial charges of bounded atoms, $\delta = \delta^+ - \delta^-$, d is the bond length in Angstroms.

The problem with this historical definition stems from the estimation of atomic partial charges. At present, such estimation relies on using first-principles calculations that are non-trivial due to the self-interaction error and require complex calculations within constrained DFT [59–61] and the kind of chosen atomic partition can also be source of errors as underestimation or overestimation [60]. It would be desirable to determine the bond dipole moments *a priori* from a simpler perspective, in order to predict more straightforwardly new functionalized multilayers with desired characteristics that strictly depend on the electron density distribution at the surface.

Thus, we have tested the possibility to correlate the difference between the electronegativities of two atoms, ΔX_{AB}, with their supposed bond dipole moment. Here, we have looked for a correlation

between the ΔX_{AB} coming from the Tantardini-Oganov[62] thermochemical electronegativity scale and bond dipole moment. We estimate the bond dipole moment in terms of ΔX_{AB} as:

$$\mu_{TO} = \Delta X_{AB} \cdot \left(\frac{d_{\text{Å}}}{a_0}\right)$$

where ΔX_{AB} is multiplied by the bond distance in Angstroms, $d_{\text{Å}}$, divided by the Bohr radius, a_0, in Angstroms, which is equal to 0.529177 Å. This allows us to use dimensionless values for bond dipole moments.

We have tested our formula on molecules containing hydrogen atoms to see if our approach is applicable. Since we selected only neutral diatomic molecules, where $\delta^+$is by nature equal to -δ^- the estimated bond dipoles μ_{TO} may be rigorously compared with the experimental or calculated dipole moments. The latter, obtained from the calculated wavefunction as an average of the **r** operator, may be also roughly estimated using atomic charges obtained from the same wavefunction and using some basis set or real space partition criterion. Results shown in **Table 1** confirm our suggestion to use μ_{TO} as semi-quantitative predictor for (bond) dipole moment.

Table 1. Bond length, electronegativity difference, calculated and measured dipole moment for several molecules with hydrogen. $\mu_{Bader}(CC)$ *is calculated in this work, while* $\mu_{Bader}\ (VASP)$ *is from Ref.*[62]

diatomic molecule	$d_{\text{Å}}$	ΔX_{AB}	μ_{TO}	μ_D / (D)	μ_{wf} / (D)	$\mu_{Bader}(CC)$/ (D)	$\mu_{Bader}\ (VASP)$/ (D)[62]
HF	0.9200	0.96	1.67	1.82[63]	1.93	3.56	3.18[62]
HCl	1.2700	0.5	1.20	1.08[63]	1.19	1.95	2.32[62]
HBr	1.4100	0.41	1.09	0.82[63]	0.89	1.15	2.84[62]
HI	1.6100	0.16	0.49	0.44[63]	0.52	0.85	3.40[62]

The value of μ_{TO} are seen within 10%-30% of those taken from NIST database[63] corresponding to experimental measured values in Debye, μ_D, and within 10%-20% of those obtained from our coupled cluster wavefunction calculations (μ_{wf}) using single doubled and triple excitation and a triple ζ local basis set. Dipole moments simply approximated from Bader charges with plane waves basis set in VASP package ($\mu_{Bader}\ (VASP)$ from Ref.[62]) greatly overestimate the experimental ones. Though a bit closer to the NIST database values, also the dipole moments calculated from Bader charges obtained from the coupled cluster wavefunction are much larger than boh those from experiment and those calculated directly from the wavefunction. This is not at all surprising since to reconstruct exactly the wavefunction dipole moment one has to add to the considered charge transfer contribution also that due to the atomic dipoles that in the case of systems with large ionic

character is opposite in sign and of the same order of magnitude of the charge transfer contribution[64,65]

It is noteworthy that it is possible to introduce a "semi-quantitative" instrument to determine *a priori* the bond dipole moment by simply using a pen and paper with Tantardini-Oganov electronegativity without complex quantum chemical calculations.

Thus, simply knowing the geometry of the system and the difference of electronegativity between two bound atoms, it is possible to define their bond dipole moment. In fact, the distance between two bound atoms assumes the meaning of weight of electronic cloud distribution between two atoms.

We have then estimated μ_{TO} between carbon and hydrogen/fluorine atoms for our diamanes showing that in case of surface and bulk states for hydrogenated and fluorinated diamanes, respectively, the dipole moment does not change with increasing the number of layers (see Table S11, S12 in Supporting Information). However, if we define the surface dipole moment as the average of μ_{TO} between the adatoms of the surface and the surface carbon atoms, then we can describe the polarization at the surface after functionalization.

Here, we observed that the average of μ_{TO} is ~2.5 for all fluorinated diamanes, while it is only ~0.2 for hydrogenated ones. The strongest dipole moment present on the fluorinated diamanes surfaces can be also considered responsible for the linear behavior of work function and in the observed range the saturation is not achieved. Nevertheless, the lowest surface dipole moment of hydrogenated diamanes allows them to achieve faster the saturation making them a better candidate for FED.

Conclusions

Our first-principles investigation of the direct and fundamental band gaps of hydrogenated and fluorinated diamanes, which represent two successful cases of reversible chemical doping, showed a behavior compatible with the formation of occupied surface electronic states for hydrogenated diamanes but no such surface states for fluorinated diamanes. The Bader analysis allowed us to corroborate this view through the study of the electronic population at the VBM. The nature of band gap behavior is responsible for the changes of work function, namely bulk electronic states in hydrogenated diamanes are correlated with the small values of work function, that are rapidly saturating with increase of the number of layers, while surface electronic states in fluorinated diamanes deliver a large work function, that is also observed to decrease slowly with increasing the number of layers with exception of fluorinated (110) and $(\bar{2}110)$. It is noteworthy that H-$(\bar{2}110)$ is the most suitable surface for FED. We have also been able to correlate the Tantardini-

Oganov electronegativity scale with the bond dipole moment showing the extension of such approach to condensed matter and envisaging the possibility to avoid expensive first-principles calculations and a priori make a prediction on surface reactivity.

Methods

Computational details

Structure relaxations and total energy calculations were performed using the optimized norm-conserving Vanderbilt pseudopotentials (ONCVP) [66,67] and the generalized gradient approximation (GGA) with the Perdew−Burke−Ernzerhof (PBE) exchange-correlation density functional [68] as implemented in Abinit ver. 9.0.4. [69,70]. Optimized norm-conserving Vanderbilt pseudopotentials (ONCVP) were adopted with 4, 1, and 7 valence electrons for carbon, hydrogen, and fluorine atoms respectively. The geometry optimization relies on Broyden-Fletcher-Goldfarb-Shanno (BFGS)[71–74] algorithm with convergence cut-off of $5.0 \cdot 10^{-5}$ Ha/bohr for the maximum net force on atoms, while the self-consistent field convergence criteria is based on residual potential cut-off equal to 10^{-12} Ha. A plane wave energy cut-off of 50 Ha and Fermi-Dirac smearing of electronic occupations equal to 0.001 Ha ensures the convergence of total energies. The Γ-centered *k*-point meshes of 6×6×1 for diamanes and 6×6×6 for bulk diamond and lonsdaleite were used for the first Brillouin zone sampling.

G_0W_0 and KS electronic band structure calculations were performed with norm-conserving relativistic separable dual-space Gaussian pseudo-potentials (HGH)[75], having the same number of valence electrons adopted in the ONCVP pseudopotentials. KS electronic structures were calculated using TB09 and PBE exchange-correlation functional [50]. For G_0W_0 calculations, the number of unoccupied bands per atom is 50 and the energy cut-off for the dielectric matrix is 5 Ha, that guarantees a band gap convergence on the order of 2 *meV*. G_0W_0 calculations for the multilayers were performed considering the Coulomb singularity problem that happens at $\mathbf{G} = 0$ and that hinders the convergence with respect to the number of *k*-points used to sample the first Brillouin zone, thanks to the Ismail-Beigi methodology[76]. These calculations were performed considering the degeneracy of bands at the valence band maxima (VBM) and conduction band minima (CBM) looking for the *GW*@TB09 band gap as the difference between the two degenerate bands at VBM and the two degenerate bands at the CBM.

No attempt was made to perform self-consistent *GW* calculations. Instead, calculations relied on the DFT electronic charge densities throughout. The electronic charge density change from such self-consistent *GW* with respect to the DFT one is not large anyhow, the variation being on the order of a millielectron per atomic unit, as reported in Ref.[77] . Thus, electronic charge densities at

386 the VBM showed throughout are KS TB09 ones.

387 The planewave-based multilayer calculations, with an inherent artificial periodicity perpendicular
388 to the multilayer, were performed without adding a planar dipole layer in the vacuum region[78],
389 because all the slabs are hydrogenated (or fluorinated) on both sides of the slab, equally, so, their
390 surface dipole long range effects cancel each other and there is no long-range buildup of electric
391 field due to these surface dipoles, in the ground-state.

392 The work function was determined as the difference of energy between the highest occupied state
393 and the vacuum level, the latter obtained by the macroscopic average technique of Baldereschi et
394 al. [79]. The highest state energy was the one from *GW*@PBE calculation, following the so-called
395 *GW*-VBM approach, see Eq.(3) of Ref. [80]. Results were compared with the uncorrected PBE values
396 in the supplementary information.

397 The electronic charge density for test molecules (see Table 1) was calculated with coupled-cluster
398 single double and third excitations using Gaussian local basis sets aug-cc-pVTZ (all-electrons
399 triple ζ basis set with diffusive and polarized) for hydrogen, fluorine and chlorine atoms[81], while
400 aug-cc-pwCVTZ-PP (relativistic triple ζ basis set with diffusive and polarized) was used for
401 bromine and iodine atoms atoms[82,83]. Their molecular geometries were taken from experimental
402 data[63] and shown in the Table 1 of the main text together with experimental dipole moments. The
403 threshold energy of SC convergence was chosen to be 10^{-8} Ha.

404 All first-principles and quasiparticle calculations on solids were performed with Abinit [69,70]. The
405 post-Hatree-Fock calculations on molecules were performed using Gaussian G16 version [84] The
406 Bader analysis was performed using CRITIC2 program. [85] The crystal structures were visualized
407 using the VESTA software[86].

408

409 ## Supporting Information

410 Supporting Information is available online and contains details of the atomic structure of studied
411 diamanes films, of the electronic band structures, of the dependency of direct and fundamental
412 band gaps as a function of the layer thickness, calculated by using the TB09 approach, and the
413 charge density coming from various atomic basins at the valence band maximum and inner bands.

414

415 ## Acknowledgment

416 The authors would like to thank Alberto Otero de-la-Roza from University of Oviedo, Davide
417 Ceresoli from CNR-SCITEC Milano and Matteo Giantomassi from UCLouvain for useful
418 discussion. This work has been supported by the Federal government of Belgium through the EoS

Project ID 40007525, the NOMAD2, INFRAEDI-05-2020 Integrated Infrastructure Initiative funded by the EU HORIZON 2020, Grant Agreement 951786. T.A. and B.I.Y. acknowledge the Taif University Research Support Project (TURSP-HC2022/1, Saudi Arabia). Ch.T. performed the calculations on resources provided by Sigma2 – The National Infrastructure for High Performance Computing Data Storage in Norway.

References

(1) Awan, T. I.; Bashir, A.; Tehseen, A. *Chemistry of Nanomaterials: Fundamentals and Applications*, 1st edition.; Elsevier: Amsterdam, Netherlands ; Cambridge, MA, 2020.

(2) Talin, A. A.; Dean, K. A.; Jaskie, J. E. Field Emission Displays: A Critical Review. *Solid-State Electronics* **2001**, *45* (6), 963–976. https://doi.org/10.1016/S0038-1101(00)00279-3.

(3) Choi, W. B.; Chung, D. S.; Kang, J. H.; Kim, H. Y.; Jin, Y. W.; Han, I. T.; Lee, Y. H.; Jung, J. E.; Lee, N. S.; Park, G. S.; Kim, J. M. Fully Sealed, High-Brightness Carbon-Nanotube Field-Emission Display. *Appl. Phys. Lett.* **1999**, *75* (20), 3129–3131. https://doi.org/10.1063/1.125253.

(4) Kim, J. M.; Choi, W. B.; Lee, N. S.; Jung, J. E. Field Emission from Carbon Nanotubes for Displays. *Diamond and Related Materials* **2000**, *9* (3), 1184–1189. https://doi.org/10.1016/S0925-9635(99)00266-6.

(5) Saito, Y.; Uemura, S. Field Emission from Carbon Nanotubes and Its Application to Electron Sources. *Carbon* **2000**, *38* (2), 169–182. https://doi.org/10.1016/S0008-6223(99)00139-6.

(6) Patra, A.; More, M. A.; Late, D. J.; Rout, C. S. Field Emission Applications of Graphene-Analogous Two-Dimensional Materials: Recent Developments and Future Perspectives. *J. Mater. Chem. C* **2021**, *9* (34), 11059–11078. https://doi.org/10.1039/D1TC02054D.

(7) Novoselov, K. S. Electric Field Effect in Atomically Thin Carbon Films. *Science* **2004**, *306* (5696), 666–669. https://doi.org/10.1126/science.1102896.

(8) Novoselov, K. S.; Andreeva, D. V.; Ren, W.; Shan, G. Graphene and Other Two-Dimensional Materials. *Front. Phys.* **2019**, *14* (1), 13301. https://doi.org/10.1007/s11467-018-0835-6.

(9) Chernozatonskii, L. A.; Sorokin, P. B.; Kvashnin, A. G.; Kvashnin, D. G. Diamond-like C2H Nanolayer, Diamane: Simulation of the Structure and Properties. *JETP Letters* **2009**, *90* (2), 134–138. https://doi.org/10.1134/S0021364009140112.

(10) Chernozatonskii, L. A.; Sorokin, P. B.; Kuzubov, A. A.; Sorokin, B. P.; Kvashnin, A. G.; Kvashnin, D. G.; Avramov, P. V.; Yakobson, B. I. Influence of Size Effect on the Electronic and Elastic Properties of Diamond Films with Nanometer Thickness. *J. Phys. Chem. C* **2011**, *115* (1), 132–136.

(11) Sivek, J.; Leenaerts, O.; Partoens, B.; Peeters, F. M. First-Principles Investigation of Bilayer Fluorographene. *The Journal of Physical Chemistry C* **2012**, *116* (36), 19240–19245. https://doi.org/10.1021/jp3027012.

(12) Kvashnin, A. G.; Sorokin, P. B. Lonsdaleite Films with Nanometer Thickness. *J. Phys. Chem. Lett.* **2014**, *5*, 541–548.

(13) Kvashnin, A. G.; Chernozatonskii, L. A.; Yakobson, B. I.; Sorokin, P. B. Phase Diagram of Quasi-Two-Dimensional Carbon, From Graphene to Diamond. *Nano Lett.* **2014**, *14*, 676–681.

(14) Antipina, L. Yu.; Sorokin, P. B. Converting Chemically Functionalized Few-Layer Graphene to Diamond Films: A Computational Study. *J. Phys. Chem. C* **2015**, *119* (5), 2828–2836. https://doi.org/DOI - 10.1021/jp510390b.

(15) Kvashnin, A. G.; Avramov, P. V.; Kvashnin, D. G.; Chernozatonskii, L. A.; Sorokin, P. B. Features of Electronic, Mechanical, and Electromechanical Properties of Fluorinated Diamond Films of Nanometer Thickness. *The Journal of Physical Chemistry C* **2017**, *121* (51), 28484–28489. https://doi.org/10.1021/acs.jpcc.7b07946.

(16) Chernozatonskii, L. A.; Demin, V. A.; Kvashnin, D. G. Fully Hydrogenated and Fluorinated Bigraphenes–Diamanes: Theoretical and Experimental Studies. *J. Carbon Res. C* **2021**, *7* (1), 17. https://doi.org/10.3390/c7010017.

(17) Sorokin, P. B.; Yakobson, B. I. Two-Dimensional Diamond—Diamane: Current State and Further Prospects. *Nano Lett.* **2021**, *21* (13), 5475–5484. https://doi.org/10.1021/acs.nanolett.1c01557.
(18) Chernozatonskii, L. A.; Demin, V. A.; Kvashnin, D. G. Ultrawide-Bandgap Moiré Diamanes Based on Bigraphenes with the Twist Angles Θ ∼ 30°. *Appl. Phys. Lett.* **2020**, *117* (25), 253104. https://doi.org/10.1063/5.0027839.
(19) Chernozatonskii, L. A.; Katin, K. P.; Demin, V. A.; Maslov, M. M. Moiré Diamanes Based on the Hydrogenated or Fluorinated Twisted Bigraphene: The Features of Atomic and Electronic Structures, Raman and Infrared Spectra. *Applied Surface Science* **2021**, *537*, 148011. https://doi.org/10.1016/j.apsusc.2020.148011.
(20) Chernozatonskii, L. A.; Demin, V. A.; Kvashnin, D. G. Moiré Diamones: New Diamond-like Films of Semifunctionalized Twisted Graphene Layers. *J. Phys. Chem. Lett.* **2022**, *13* (24), 5399–5404. https://doi.org/10.1021/acs.jpclett.2c00948.
(21) Chernozatonskii, L. A.; Demin, V. A. Diamond-Like Films from Twisted Few-Layer Graphene. *Jetp Lett.* **2022**, *115* (3), 161–166. https://doi.org/10.1134/S0021364022030043.
(22) Tiwari, S. K.; Pandey, R.; Wang, N.; Kumar, V.; Sunday, O. J.; Bystrzejewski, M.; Zhu, Y.; Mishra, Y. K. Progress in Diamanes and Diamanoids Nanosystems for Emerging Technologies. *Advanced Science n/a* (n/a), 2105770. https://doi.org/10.1002/advs.202105770.
(23) Chernozatonskii, L. A.; Demin, V. A.; Kvashnin, A. G.; Kvashnin, D. G. Diamane Quasicrystals. *Applied Surface Science* **2022**, *572*, 151362. https://doi.org/10.1016/j.apsusc.2021.151362.
(24) Piazza, F.; Gough, K.; Monthioux, M.; Puech, P.; Gerber, I.; Wiens, R.; Paredes, G.; Ozoria, C. Low Temperature, Pressureless Sp2 to Sp3 Transformation of Ultrathin, Crystalline Carbon Films. *Carbon* **2019**, *145*, 10–22. https://doi.org/10.1016/j.carbon.2019.01.017.
(25) Piazza, F.; Kelvin Cruz; Monthioux, M.; Puech, P.; Gerber, I. Raman Evidence for the Successful Synthesis of Diamane. *Carbon* **2020**, *169*, 129–133. https://doi.org/10.1016/j.carbon.2020.07.068.
(26) Zhu, L.; Zhang, T. Suppressed Thermal Conductivity in Fluorinated Diamane: Optical Phonon Dominant Thermal Transport. *Appl. Phys. Lett.* **2019**, *115* (15), 151904. https://doi.org/10.1063/1.5123195.
(27) Zhu, L.; Li, W.; Ding, F. Giant Thermal Conductivity in Diamane and the Influence of Horizontal Reflection Symmetry on Phonon Scattering. *Nanoscale* **2019**, *11* (10), 4248–4257. https://doi.org/10.1039/C8NR08493A.
(28) Zhang, T.; Zhu, L. Sensitively Tuning the Thermal Conductivity of Diamane via Engineering the Mass of Functional Groups. *Nanotechnology* **2020**, *31* (43), 435409. https://doi.org/10.1088/1361-6528/aba5b8.
(29) Raeisi, M.; Mortazavi, B.; Podryabinkin, E. V.; Shojaei, F.; Zhuang, X.; Shapeev, A. V. High Thermal Conductivity in Semiconducting Janus and Non-Janus Diamanes. *Carbon* **2020**, *167*, 51–61. https://doi.org/10.1016/j.carbon.2020.06.007.
(30) Zheng, Z.; Zhan, H.; Nie, Y.; Xu, X.; Qi, D.; Gu, Y. Single Layer Diamond - A New Ultrathin 2D Carbon Nanostructure for Mechanical Resonator. *Carbon* **2020**, *161*, 809–815. https://doi.org/10.1016/j.carbon.2020.02.017.
(31) Hu, Y.; Li, D.; Yin, Y.; Li, S.; Ding, G.; Zhou, H.; Zhang, G. The Important Role of Strain on Phonon Hydrodynamics in Diamond-like Bi-Layer Graphene. *Nanotechnology* **2020**, *31* (33), 335711. https://doi.org/10.1088/1361-6528/ab8ee1.
(32) Gupta, S.; Yang, J.-H.; Yakobson, B. I. Two-Level Quantum Systems in Two-Dimensional Materials for Single Photon Emission. *Nano Letters* **2019**, *19* (1), 408–414. https://doi.org/10.1021/acs.nanolett.8b04159.
(33) Qiu, D.; Wang, Q.; Cheng, S.; Gao, N.; Li, H. Electronic Structures of Two-Dimensional Hydrogenated Bilayer Diamond Films with Si Dopant and Si-V Center. *Results in Physics* **2019**, *13*, 102240. https://doi.org/10.1016/j.rinp.2019.102240.
(34) Li, J.; Yin, H.; Gao, N.; Zhang, M.; Mu, J.; Gao, L.; Li, H. First-Principles Calculations for Li, P Dopants and Vacancy Defect in Ultra-Thin Hydrogenated Diamond Nanofilms: Structural, Electronic and Optical Properties. *Diamond and Related Materials* **2019**, *99*, 107526. https://doi.org/10.1016/j.diamond.2019.107526.

(35) Gierster, L.; Vempati, S.; Stähler, J. Ultrafast Generation and Decay of a Surface Metal. *Nat Commun* **2021**, *12* (1), 978. https://doi.org/10.1038/s41467-021-21203-6.
(36) Elias, D. C.; Nair, R. R.; Mohiuddin, T. M. G.; Morozov, S. V.; Blake, P.; Halsall, M. P.; Ferrari, A. C.; Boukhvalov, D. W.; Katsnelson, M. I.; Geim, A. K.; Novoselov, K. S. Control of Graphene's Properties by Reversible Hydrogenation: Evidence for Graphane. *Science (New York, N.Y.)* **2009**, *323*, 610–613.
(37) Luo, Z.; Yu, T.; Kim, K.; Ni, Z.; You, Y.; Lim, S.; Shen, Z.; Wang, S.; Lin, J. Thickness-Dependent Reversible Hydrogenation of Graphene Layers. *ACS Nano* **2009**, *3* (7), 1781–1788.
(38) Ryu, S.; Han, M. Y.; Maultzsch, J.; Heinz, T. F.; Kim, P.; Steigerwald, M. L.; Brus, L. E. Reversible Basal Plane Hydrogenation of Graphene. *Nano letters* **2008**, *8* (12), 4597–4602.
(39) Whitener, K. E.; Lee, W. K.; Campbell, P. M.; Robinson, J. T.; Sheehan, P. E. Chemical Hydrogenation of Single-Layer Graphene Enables Completely Reversible Removal of Electrical Conductivity. *Carbon* **2014**, *72*, 348–353. https://doi.org/10.1016/j.carbon.2014.02.022.
(40) Yang, H.; Chen, M.; Zhou, H.; Qiu, C.; Hu, L.; Yu, F.; Chu, W.; Sun, S.; Sun, L. Preferential and Reversible Fluorination of Monolayer Graphene. *J. Phys. Chem. C* **2011**, *115* (34), 16844–16848. https://doi.org/10.1021/jp204573z.
(41) Cheng, S.-H.; Zou, K.; Okino, F.; Gutierrez, H. R.; Gupta, A.; Shen, N.; Eklund, P. C.; Sofo, J. O.; Zhu, J. Reversible Fluorination of Graphene: Evidence of a Two-Dimensional Wide Bandgap Semiconductor. *Phys. Rev. B* **2010**, *81* (20), 205435. https://doi.org/10.1103/PhysRevB.81.205435.
(42) Cheng, L.; Jandhyala, S.; Mordi, G.; Lucero, A. T.; Huang, J.; Azcatl, A.; Addou, R.; Wallace, R. M.; Colombo, L.; Kim, J. Partially Fluorinated Graphene: Structural and Electrical Characterization. *ACS Appl. Mater. Interfaces* **2016**, *8* (7), 5002–5008. https://doi.org/10.1021/acsami.5b11701.
(43) Fan, K.; Liu, J.; Liu, Y.; Liu, X.; Wang, X. Phase Reversal Behavior on Two-Dimension Plane of Fluorinated Graphene during Defluorination. *Carbon* **2021**, *183*, 660–671. https://doi.org/10.1016/j.carbon.2021.07.060.
(44) Erohin, S. V.; Ruan, Q.; Sorokin, P. B.; Yakobson, B. I. Nano-Thermodynamics of Chemically Induced Graphene–Diamond Transformation. *Small* **2020**, *16* (47), 2004782. https://doi.org/10.1002/smll.202004782.
(45) Hedin, L. New Method for Calculating the One-Particle Green's Function with Application to the Electron-Gas Problem. *Phys. Rev.* **1965**, *139* (3A), A796–A823. https://doi.org/10.1103/PhysRev.139.A796.
(46) Bader, R. F. W. *Atoms in Molecules: A Quantum Theory*; International Series of Monographs on Chemistry; Oxford University Press: Oxford, New York, 1994.
(47) Tantardini, C.; Ceresoli, D.; Benassi, E. Source Function and Plane Waves: Toward Complete Bader Analysis. *Journal of Computational Chemistry* **2016**, *37* (23), 2133–2139. https://doi.org/10.1002/jcc.24433.
(48) Tikhomirova, K. A.; Tantardini, C.; Sukhanova, E. V.; Popov, Z. I.; Evlashin, S. A.; Tarkhov, M. A.; Zhdanov, V. L.; Dudin, A. A.; Oganov, A. R.; Kvashnin, D. G.; Kvashnin, A. G. Exotic Two-Dimensional Structure: The First Case of Hexagonal NaCl. *J. Phys. Chem. Lett.* **2020**, *11* (10), 3821–3827. https://doi.org/10.1021/acs.jpclett.0c00874.
(49) Tantardini, C.; Kvashnin, A. G.; Gatti, C.; Yakobson, B. I.; Gonze, X. Computational Modeling of 2D Materials under High Pressure and Their Chemical Bonding: Silicene as Possible Field-Effect Transistor. *ACS Nano* **2021**, *15* (4), 6861–6871. https://doi.org/10.1021/acsnano.0c10609.
(50) Tran, F.; Blaha, P. Accurate Band Gaps of Semiconductors and Insulators with a Semilocal Exchange-Correlation Potential. *Phys. Rev. Lett.* **2009**, *102* (22), 226401. https://doi.org/10.1103/PhysRevLett.102.226401.
(51) Tantardini, C.; Gonze, X. Band Gap Bowing and Spectral Width of Ga(1−x)InxN Alloys for Modelling Light Emitting Diodes. *Physica B: Condensed Matter* **2021**, 413481. https://doi.org/10.1016/j.physb.2021.413481.
(52) Waroquiers, D.; Lherbier, A.; Miglio, A.; Stankovski, M.; Poncé, S.; Oliveira, M. J. T.; Giantomassi, M.; Rignanese, G.-M.; Gonze, X. Band Widths and Gaps from the Tran-Blaha Functional:

Comparison with Many-Body Perturbation Theory. *Phys. Rev. B* **2013**, *87* (7), 075121. https://doi.org/10.1103/PhysRevB.87.075121.
(53) Borlido, P.; Aull, T.; Huran, A. W.; Tran, F.; Marques, M. A. L.; Botti, S. Large-Scale Benchmark of Exchange–Correlation Functionals for the Determination of Electronic Band Gaps of Solids. *J. Chem. Theory Comput.* **2019**, *15* (9), 5069–5079. https://doi.org/10.1021/acs.jctc.9b00322.
(54) Helmholtz, H. Ueber Einige Gesetze Der Vertheilung Elektrischer Ströme in Körperlichen Leitern Mit Anwendung Auf Die Thierisch-Elektrischen Versuche. *Annalen der Physik* **1853**, *165* (6), 211–233. https://doi.org/10.1002/andp.18531650603.
(55) Ehrenstein, G.; Gilbert, D. L. Evidence for Membrane Surface from Measurement of Potassium Kinetics as a Function of External Divalent Cation Concentration. *Biophys J* **1973**, *13* (5), 495–497. https://doi.org/10.1016/S0006-3495(73)86002-3.
(56) Grahame, D. C. The Electrical Double Layer and the Theory of Electrocapillarity. *Chem. Rev.* **1947**, *41* (3), 441–501. https://doi.org/10.1021/cr60130a002.
(57) Stern, O. Zur Theorie Der Elektrolytischen Doppelschicht. *Zeitschrift für Elektrochemie und angewandte physikalische Chemie* **1924**, *30* (21–22), 508–516. https://doi.org/10.1002/bbpc.192400182.
(58) Pauling, L. THE NATURE OF THE CHEMICAL BOND. IV. THE ENERGY OF SINGLE BONDS AND THE RELATIVE ELECTRONEGATIVITY OF ATOMS. *J. Am. Chem. Soc.* **1932**, *54* (9 DOI-10.1021/ja01348a011), 3570–3582.
(59) Dederichs, P. H.; Blügel, S.; Zeller, R.; Akai, H. Ground States of Constrained Systems: Application to Cerium Impurities. *Phys. Rev. Lett.* **1984**, *53* (26), 2512–2515. https://doi.org/10.1103/PhysRevLett.53.2512.
(60) Kaduk, B.; Kowalczyk, T.; Van Voorhis, T. Constrained Density Functional Theory. *Chem. Rev.* **2012**, *112* (1), 321–370. https://doi.org/10.1021/cr200148b.
(61) Gonze, X.; Seddon, B.; Elliott, J. A.; Tantardini, C.; Shapeev, A. V. Constrained Density Functional Theory: A Potential-Based Self-Consistency Approach. *J. Chem. Theory Comput.* **2022**, *18* (10), 6099–6110. https://doi.org/10.1021/acs.jctc.2c00673.
(62) Tantardini, C.; Oganov, A. R. Thermochemical Electronegativities of the Elements. *Nat Commun* **2021**, *12* (1), 2087. https://doi.org/10.1038/s41467-021-22429-0.
(63) Diatomic Spectral Database. *NIST* **2009**.
(64) Bader, R. F. W.; Larouche, A.; Gatti, C.; Carroll, M. T.; MacDougall, P. J.; Wiberg, K. B. Properties of Atoms in Molecules: Dipole Moments and Transferability of Properties. *J. Chem. Phys.* **1987**, *87* (2), 1142–1152. https://doi.org/10.1063/1.453294.
(65) Gatti, C.; Saunders, V. R.; Roetti, C. Crystal Field Effects on the Topological Properties of the Electron Density in Molecular Crystals: The Case of Urea. *J. Chem. Phys.* **1994**, *101* (12), 10686–10696. https://doi.org/10.1063/1.467882.
(66) Hamann, D. R. Optimized Norm-Conserving Vanderbilt Pseudopotentials. *Phys. Rev. B* **2013**, *88* (8), 085117. https://doi.org/10.1103/PhysRevB.88.085117.
(67) van Setten, M. J.; Giantomassi, M.; Bousquet, E.; Verstraete, M. J.; Hamann, D. R.; Gonze, X.; Rignanese, G.-M. The PseudoDojo: Training and Grading a 85 Element Optimized Norm-Conserving Pseudopotential Table. *Computer Physics Communications* **2018**, *226*, 39–54. https://doi.org/10.1016/j.cpc.2018.01.012.
(68) Perdew, J. P.; Burke, K.; Ernzerhof, M. Generalized Gradient Approximation Made Simple. *Phys. Rev. Lett.* **1997**, *78* (7), 1396–1396.
(69) Gonze, X.; Jollet, F.; Abreu Araujo, F.; Adams, D.; Amadon, B.; Applencourt, T.; Audouze, C.; Beuken, J.-M.; Bieder, J.; Bokhanchuk, A.; Bousquet, E.; Bruneval, F.; Caliste, D.; Côté, M.; Dahm, F.; Da Pieve, F.; Delaveau, M.; Di Gennaro, M.; Dorado, B.; Espejo, C.; Geneste, G.; Genovese, L.; Gerossier, A.; Giantomassi, M.; Gillet, Y.; Hamann, D. R.; He, L.; Jomard, G.; Laflamme Janssen, J.; Le Roux, S.; Levitt, A.; Lherbier, A.; Liu, F.; Lukačević, I.; Martin, A.; Martins, C.; Oliveira, M. J. T.; Poncé, S.; Pouillon, Y.; Rangel, T.; Rignanese, G.-M.; Romero, A. H.; Rousseau, B.; Rubel, O.; Shukri, A. A.; Stankovski, M.; Torrent, M.; Van Setten, M. J.; Van Troeye, B.; Verstraete, M. J.; Waroquiers, D.; Wiktor, J.; Xu, B.; Zhou, A.; Zwanziger, J. W. Recent Developments in the ABINIT

Software Package. *Computer Physics Communications* **2016**, *205*, 106–131. https://doi.org/10.1016/j.cpc.2016.04.003.
(70) Gonze, X.; Amadon, B.; Antonius, G.; Arnardi, F.; Baguet, L.; Beuken, J.-M.; Bieder, J.; Bottin, F.; Bouchet, J.; Bousquet, E.; Brouwer, N.; Bruneval, F.; Brunin, G.; Cavignac, T.; Charraud, J.-B.; Chen, W.; Côté, M.; Cottenier, S.; Denier, J.; Geneste, G.; Ghosez, P.; Giantomassi, M.; Gillet, Y.; Gingras, O.; Hamann, D. R.; Hautier, G.; He, X.; Helbig, N.; Holzwarth, N.; Jia, Y.; Jollet, F.; Lafargue-Dit-Hauret, W.; Lejaeghere, K.; Marques, M. A. L.; Martin, A.; Martins, C.; Miranda, H. P. C.; Naccarato, F.; Persson, K.; Petretto, G.; Planes, V.; Pouillon, Y.; Prokhorenko, S.; Ricci, F.; Rignanese, G.-M.; Romero, A. H.; Schmitt, M. M.; Torrent, M.; van Setten, M. J.; Van Troeye, B.; Verstraete, M. J.; Zérah, G.; Zwanziger, J. W. The Abinitproject: Impact, Environment and Recent Developments. *Computer Physics Communications* **2020**, *248*, 107042. https://doi.org/10.1016/j.cpc.2019.107042.
(71) Broyden, C. G. The Convergence of a Class of Double-Rank Minimization Algorithms 1. General Considerations. *IMA J Appl Math* **1970**, *6* (1), 76–90. https://doi.org/10.1093/imamat/6.1.76.
(72) Goldfarb, D. A Family of Variable-Metric Methods Derived by Variational Means. *Math. Comp.* **1970**, *24* (109), 23–26. https://doi.org/10.1090/S0025-5718-1970-0258249-6.
(73) Shanno, D. F. Conditioning of Quasi-Newton Methods for Function Minimization. *Math. Comp.* **1970**, *24* (111), 647–656. https://doi.org/10.1090/S0025-5718-1970-0274029-X.
(74) Steihaug, T. *Practical Methods of Optimization Volume 1 : Unconstrained Optimization*; 1982.
(75) Hartwigsen, C.; Goedecker, S.; Hutter, J. Relativistic Separable Dual-Space Gaussian Pseudopotentials from H to Rn. *Phys. Rev. B* **1998**, *58* (7), 3641–3662. https://doi.org/10.1103/PhysRevB.58.3641.
(76) Ismail-Beigi, S. Truncation of Periodic Image Interactions for Confined Systems. *Phys. Rev. B* **2006**, *73* (23), 233103. https://doi.org/10.1103/PhysRevB.73.233103.
(77) Shaltaf, R.; Rignanese, G.-M.; Gonze, X.; Giustino, F.; Pasquarello, A. Band Offsets at the $\mathrm{Si}/{\mathrm{SiO}}_{2}$ Interface from Many-Body Perturbation Theory. *Phys. Rev. Lett.* **2008**, *100* (18), 186401. https://doi.org/10.1103/PhysRevLett.100.186401.
(78) Neugebauer, J.; Scheffler, M. Adsorbate-Substrate and Adsorbate-Adsorbate Interactions of Na and K Adlayers on Al(111). *Phys. Rev. B* **1992**, *46* (24), 16067–16080. https://doi.org/10.1103/PhysRevB.46.16067.
(79) Baldereschi, A.; Baroni, S.; Resta, R. Band Offsets in Lattice-Matched Heterojunctions: A Model and First-Principles Calculations for GaAs/AlAs. *Phys. Rev. Lett.* **1988**, *61* (6), 734–737. https://doi.org/10.1103/PhysRevLett.61.734.
(80) Jiang, H. Electronic Band Structures of Molybdenum and Tungsten Dichalcogenides by the GW Approach. *J. Phys. Chem. C* **2012**, *116* (14), 7664–7671. https://doi.org/10.1021/jp300079d.
(81) Kendall, R. A.; Dunning, T. H.; Harrison, R. J. Electron Affinities of the First-row Atoms Revisited. Systematic Basis Sets and Wave Functions. *J. Chem. Phys.* **1992**, *96* (9), 6796–6806. https://doi.org/10.1063/1.462569.
(82) Peterson, K. A.; Figgen, D.; Goll, E.; Stoll, H.; Dolg, M. Systematically Convergent Basis Sets with Relativistic Pseudopotentials. II. Small-Core Pseudopotentials and Correlation Consistent Basis Sets for the Post-d Group 16–18 Elements. *J. Chem. Phys.* **2003**, *119* (21), 11113–11123. https://doi.org/10.1063/1.1622924.
(83) Peterson, K. A.; Yousaf, K. E. Molecular Core-Valence Correlation Effects Involving the Post-d Elements Ga–Rn: Benchmarks and New Pseudopotential-Based Correlation Consistent Basis Sets. *J. Chem. Phys.* **2010**, *133* (17), 174116. https://doi.org/10.1063/1.3503659.
(84) Frisch, M. J.; Trucks, G. W.; Schlegel, H. B.; Scuseria, G. E.; Robb, M. A.; Cheeseman, J. R.; Scalmani, G.; Barone, V.; Petersson, G. A.; Nakatsuji, H.; Li, X.; Caricato, M.; Marenich, A. V.; Bloino, J.; Janesko, B. G.; Gomperts, R.; Mennucci, B.; Hratchian, H. P.; Ortiz, J. V.; Izmaylov, A. F.; Sonnenberg, J. L.; Williams-Young, D.; Ding, F.; Lipparini, F.; Egidi, F.; Goings, J.; Peng, B.; Petrone, A.; Henderson, T.; Ranasinghe, D.; Zakrzewski, V. G.; Gao, J.; Rega, N.; Zheng, G.; Liang, W.; Hada, M.; Ehara, M.; Toyota, K.; Fukuda, R.; Hasegawa, J.; Ishida, M.; Nakajima, T.; Honda, Y.; Kitao, O.; Nakai, H.; Vreven, T.; Throssell, K.; Montgomery, J. A., Jr.; Peralta, J. E.; Ogliaro, F.; Bearpark, M. J.; Heyd, J. J.; Brothers, E. N.; Kudin, K. N.; Staroverov, V. N.; Keith, T. A.; Kobayashi, R.; Normand,

J.; Raghavachari, K.; Rendell, A. P.; Burant, J. C.; Iyengar, S. S.; Tomasi, J.; Cossi, M.; Millam, J. M.; Klene, M.; Adamo, C.; Cammi, R.; Ochterski, J. W.; Martin, R. L.; Morokuma, K.; Farkas, O.; Foresman, J. B.; Fox, D. J. *Gaussian 16 Revision C.01*; 2016.

(85) Otero-de-la-Roza, A.; Johnson, E. R.; Luaña, V. Critic2: A Program for Real-Space Analysis of Quantum Chemical Interactions in Solids. *Computer Physics Communications* **2014**, *185* (3), 1007–1018. https://doi.org/10.1016/j.cpc.2013.10.026.

(86) Momma, K.; Izumi, F. VESTA 3 for Three-Dimensional Visualization of Crystal, Volumetric and Morphology Data. *J Appl Cryst, J Appl Crystallogr* **2011**, *44*, 1272–1276. https://doi.org/10.1107/S0021889811038970.